Hindawi

Research Article

Functional Nanorealgar Quantum Dots with Aggregation-Induced Emission Enhancement for Tumor Neovascular-Targeted Theranostics

Shengyan Pu [iD],[1] **Wenwen Wu** [iD],[1] **Dongsheng Shi** [iD],[1] **Yanqi Dai** [iD],[1] **Jun Zhang** [iD],[1] **Mingyan Zhao** [iD],[1] **Shuangyu Liu** [iD],[1] **Guihong Zheng** [iD],[1] **Xingqi Wang** [iD],[1] **Yu Yan** [iD],[2] and **Jun Xie** [iD][1]

[1]*Key Laboratory for Biotechnology on Medicinal Plants of Jiangsu Province and Biomedical R&D Center, School of Life Science, Jiangsu Normal University, Xuzhou 221116, China*
[2]*Department of Chemistry, Bengbu Medical College, Bengbu 233030, China*

Correspondence should be addressed to Xingqi Wang; xingqiw_wjm@jsnu.edu.cn, Yu Yan; yanyu@bbmc.edu.cn and Jun Xie; xiejun@jsnu.edu.cn

Realgar, a traditional Chinese medicine, has notable antitumor activity and can be used in various hematologic tumor and solid tumor therapies in a wide range of clinical applications. Nanosized realgar possesses higher surface activity and enhanced therapeutic effects on cancer cells compared with those of bulk realgar. In this study, we reported the design of high-performance nanorealgar quantum dots (NR QDs) with aggregation-induced emission enhancement of crystal units (CUs) with the addition of hydrochloric acid. The enhanced fluorescence characteristics of NR QDs are associated with an optimized crystal structure obtained by accelerating the growth process of NR CUs in which the smaller NR CUs facilitate a self-assembling arrangement and a complete structural optimization process, ultimately forming regular crystallization with a size quantization effect. To improve the theranostic efficiency of NR QDs, we synthesized NR QDs coupled with a tripeptide of arginine–glycine–aspartic acid (RGD) with tumor neovascular targeting. We intravenously injected NR@RGD QDs into BALB/c mice bearing a subcutaneously transplanted breast tumor (4T1). Our results indicate that functional NR@RGD QDs are effective chemotherapeutic drugs that can anchor into the tumor endothelial cells through an active targeting effect, inhibit the angiogenesis in the tumor, and eventually "cut-off" the nutrient-rich blood supply to the tumor. This promising antiangiogenesis therapeutic strategy induces NR@RGD QDs to penetrate tumor-fenestrated vascular networks and has potential clinical value.

1. Introduction

Breast carcinoma is one of the most common malignant tumors that threatens the lives and health of women worldwide [1]. Typically, chemotherapy is an effective assistant treatment for patients with breast carcinoma after surgery and radiotherapy, which can mop up residual cancer cells that can spread to other organs in the body. However, the overuse of traditional chemotherapeutic drugs can lead to significant drug resistance and poor patient tolerance. In such cases, new drug development or optimized design in the pharmaceutical dosage form of traditional medicines (TMs) can

help tackle the metastasis and the recurrence of tumors and improve the effectiveness of chemotherapy.

Realgar (arsenic sulfide, As_4S_4) as a traditional Chinese medicine (TCM) and toxic arsenical agent has a history of more than 2,000 years in mineral medicine. Its therapeutic effects are mainly due to the active ingrdients in the mineral substances. Realgar has remarkable therapeutic effects on various malignancies, including hematopoietic tumors (e.g., acute promyelocytic leukemia, APL) and solid malignancies (e.g., glioma and breast carcinoma) [2–5]. Basic and clinical research have indicated that realgar is safe and effective for remission induction and maintenance therapy in patients

with APL, which are significant for improving hematopoietic functions in patients [2, 3]. Nevertheless, the poor water dispersibility, low organism-absorbing ability, and high liver/kidney acute toxicity of bulk realgar may lead to low bioavailability and medication safety, limiting its use in practical biomedicine. The development of safe, highly efficient, and low-toxicity realgar agents has recently attracted attention in the field of clinical medicine.

One way to overcome these limitations is to design a new nanorealgar (NR) with high performance. Miniaturizing the drugs can dramatically increase stability and the success of drug delivery, allow the quantitative monitoring of drug uptake by tumors, and simultaneously improve the pharmacotherapy efficacy while reducing adverse drug reactions. In recent years, the rapid development of nanotechnology has opened up new areas of biological application of inorganic nanomaterials with controllable size, shape, and surface modification in medical imaging (e.g., fluorescence imaging, computed tomography (CT) imaging, magnetic resonance imaging, and photoacoustic tomography) diagnosis and therapies (e.g., photothermal therapy, photodynamic therapy, chemodynamic therapy, and magnetic induction hyperthermia (MIH)) [6–13]. Recent studies have shown that the nanoscale process in bulk realgar offers the possibility of catering to the demand for enhancing its surface activity and antitumor activity [4, 5, 14–19]. Generally, NR was mainly prepared using mechanical comminuting and hot-melt extrusion processes [15, 16]. However, the limitations of these approaches are the broad particle size distribution and poor stability of the synthesized NR particles, thus hindering their efficient clinical usage.

Early studies have shown that bulk realgar is well dispersed in liquid ammonia or anhydrous amines owing to chemical chelation between nitrogen atoms (existing in amine groups) and arsenic atoms (existing in realgar) [20–22]. In our previous study, we found that when the realgar particle size was decreased to the ultrafine nanometer scale (~3 nm), it displayed excellent fluorescence properties (in the 600–725 nm emission range) resembling quantum dots (QDs), as well as superior biocompatibility and antitumor activity [22]. Based on the results of the previous study, a novel method for the synthesis of high-performance NR QDs was explored in the present study. Bulk realgar powder (RP) was initially dissolved in ethanolamine (EA) solution at 80°C via a coordination chemical reaction to form NR crystal units (CUs) with a surface modification of EA (NR@EA CUs). However, EA, as an organic ligand, has poor biocompatibility and needs to be removed. Therefore, we designed aqueous NR QDs with a functionalized polyethylene glycol molecule (NH$_2$–PEG2000–COOH), which acted as a stabilizer by the ligand exchange method, and further coupled it with a tripeptide of arginine–glycine–aspartic acid (NR@RGD QDs) with tumor neovascular targeting ability. We believe that the NR@RGD QDs have utility both as an "antitumor drug" by inducing prominent chemotherapy effect and a "sustainable fluorescence probe" for enhancing active targeting efficacy and inhibiting tumor angiogenesis. This is a promising antiangiogenesis therapeutic strategy for TCM in a wide range of clinical theranostics.

2. Materials and Methods

2.1. Materials. RP (medical grade) was purchased from Xi'an Tianzheng Pharmaceutical Adjuvant Co., Ltd. (China). Functionalized NH$_2$–PEG2000–COOH was purchased from Shanghai Ponsure Biotechnology Co., Ltd. Cyclic RGD tripeptide was purchased from Shanghai Apeptide Co., Ltd. (China). EA, 2-(*N*-morpholine) ethanesulfonic acid (MES), 1-ethyl-3-(dimethylaminopropyl) carbodiimide hydrochloride (EDC), and *N*-hydroxysuccinimide (NHS) were purchased from Aladdin Chemical Reagent Co., Ltd. (China). Hydrochloric acid (HCl), ethanol, paraformaldehyde, and boric acid were purchased from Sinopharm Chemical Reagent Co., Ltd. (China). Chemical reagents used above were all analytical grade. In addition, Masson trichrome kit, terminal deoxynucleotidyl transferase dUTP nick end labeling (TUNEL) kit and rabbit anti-CD31 and Ki-67 primary antibodies were purchased from Servicebio Technology Co., Ltd. (China). Cell apoptosis detection kit and colorimetric cell counting kit 8 (CCK-8) kits were purchased from KeyGEN Biotechnology Co., Ltd. (China). Milli-Q deionized water was supplied throughout the experiments (Millipore, MA, USA).

2.2. Synthesis of Nanorealgar Quantum Dots Coupled with EA (NR@EA QDs). One gram of the highly purified RP was dispersed in 20 mL of EA solution at a high temperature (80°C), followed by a magnetic stirring for 12 hr. Then the NR@EA CUs were obtained through the chemical chelating reaction between nitrogen atom (existing in EA) and arsenic atom (existing in realgar). After the addition of 5 mL concentrated HCl, the aggregated NR CUs were precipitated from NR@EA CUs solution, and continued to reassemble and grow with a magnetic stirrer at 80°C for 48 hr, finally obtaining the NR@EA QDs with larger size.

2.3. Synthesis of NR@RGD QDs. The obtained NR@EA QDs were centrifuged (10,000 rpm) and redissolved in water. With the addition of 100 mg of NH$_2$–PEG2000–COOH acted as a stabilizer for NR complex, the mixture was then stirred fully by chemical chelating between nitrogen atom (existing in NH$_2$–PEG2000–COOH) and arsenic atom (existing in bare NR) with a magnetic stirrer at 37°C for 24 hr. After removing the insoluble precipitation by centrifugation and purifying with a 300 kDa dialysis bag to remove the free NH$_2$–PEG2000–COOH molecule, the water-soluble NR@COOH QDs solution was subsequently obtained.

In the final peptide coupling step, the NR@COOH QDs were dispersed in 20 mL MES buffer (pH 5.4, 0.02 mol·L^{-1}), mixed with 100 mg of EDC and 150 mg of NHS, and shaking incubated for 30 min at 37°C to form the active carboxyl intermediates. Subsequently, 15 mg RGD peptide was slowly added, and bound to the intermediates, incubating at 37°C for 24 hr in borate buffer (pH 8.4). The purified NR@RGD QDs solution was eventually obtained through multiple ultrafiltration centrifugation (4,000 rpm) and washing steps.

2.4. Characterization of NR@RGD QDs. The morphology, state of aggregation, and crystal size of obtained NR@RGD QDs were characterized by transmission electron microscopy (TEM, JEOL, Japan). Their size distribution in aqueous solution was measured by a nanoparticle analyzer (Malvern, UK). In optical characterization, the fluorescence spectrophotometer (Shimadzu F-7000, Japan) and fluorescence imaging system (Caliper Life Sciences, USA) were used to evaluate the fluorescence property of NR@RGD QDs at the excitation wavelength (E_x) of 570 nm and the emission wavelength (E_m) of 660 nm. The absorption spectrum of NR@RGD QDs was determined by UV–vis spectrophotometer (Shimadzu, UV-2501PC, Japan). X-ray powder diffraction (XRD, Siemens D-500) was used for phase identification and crystal structure determination of NR@RGD QDs. In addition, the chemical structure of NR@RGD QDs was recorded using an inVia Raman microscope (Renishaw, UK).

2.5. Hemolysis Assay of NR@RGD QDs. Mouse whole blood was acquired and centrifuged at 3,000 rpm for 10 min and washed with PBS buffer solution three times, ultimately getting pure erythrocytes. Subsequently, the NR@RGD QDs with various concentrations (0.1, 0.5, 1.0, 2.0, 3.0, and 5.0 μg of As·mL^{-1}) were added into the 4% erythrocytes and incubated at 37°C for 12 hr for hemolysis observation.

2.6. Cell Culture. The 4T1 (mice breast cancerous) cells, RAW 264.7 macrophages, and HUVECs (human umbilical vein endothelial cells) were supplied by Cell Bank, Chinese Academy of Sciences (Shanghai, China). The above cells were routinely cultured in Dulbecco's modified Eagle medium (DMEM, Gibco, Grand Island, NY, USA) supplement with 10% (v/v) fetal bovine serum (FBS, Gibco, Grand Island, NY, USA), and 1% (v/v) penicillin–streptomycin solution (Solarbio, Beijing, China) at 37°C in 5% CO_2 humidified atmosphere.

2.7. In Vitro Cytotoxicity Assay. The 4T1 cells were seeded in 96-well plates at a density of 5×10^4 cells per well and cultured overnight followed by incubation with different concentrations of NR@RGD QDs for 24 hr. Subsequently, 10 μL CCK-8 reagent was added into each well and coincubation with cells for 1 hr in the dark. The absorbance at 450 nm was recorded by a microplate reader (Bio Tek, Synergy H4, USA).

2.8. In Vitro Intracellular Fluorescence Imaging. The *in vitro* targeting behavior and antiphagocytosis capability of NR@RGD QDs were reflected by intracellular fluorescence imaging using a confocal laser scanning microscopy (CLSM, Leica, DMi8, Germany). In detail, the HUVECs and RAW 264.7 cells were seeded in 12-well plates (1×10^6 cells), respectively, with a diameter of 2 cm round glass slides at the bottom. After being cultured overnight, the cells were incubated with NR@RGD QDs (1.0 μg of As·mL^{-1}) for 24 hr. Then, the cells on the slides were fixed with 4% paraformaldehyde for 30 min. Subsequently, the slides were washed with PBS three times, stained with DAPI (0.02%) in the dark, and then observed under CLSM monitoring.

2.9. Cell Apoptosis. The NR@RGD QDs-induced cell apoptosis was measured by an imaging flow cytometry (IFC, Amnis, Flow sight, USA) via Annexin V-FITC/PI detection kit. The 4T1 cells were seeded in six-well plates at a density of 2×10^5 cells per well and cultured overnight. Then, the NR@RGD QDs with a concentration of 1.0 μg As·mL^{-1} were added and incubated with cells for 24 hr. The treated cells were harvested and centrifuged at 1,000 rpm for 3 min. After being washed with PBS three times, cells were resuspended in 500 μL binding buffer followed by incubation with the staining solution (500 μL Annexin V-FITC and 5 μL PI mixture) in the dark for 20 min. The fluorescence signal of cells was detected by an IFC with background subtraction. IDEAS software (version 6.2) was used to analyze the obtained data. The cell population in the lower right (LR) and upper right (UR) quadrant (Annexin V+/PI±) was commonly considered as apoptosis cells.

2.10. Cell Cycle Arrest. The NR@RGD QDs-induced cell cycle arrest was evaluated by a cell cycle detection kit. 4T1 cells were seeded in six-well plates at a density of 2×10^5 cells per well and cultured for 24 hr. Then, cells were coincubation with added NR@RGD QDs (1.0 μg As·mL^{-1}) for 24 hr. After being washed with PBS three times, the trypsin-digested cells were centrifuged (1,000 rpm, 3 min) to remove the supernatant. The collected cells were fixed with 500 μL cold ethanol (70%) at 4°C for 12 hr. Then, the cells were centrifuged at 2,000 rpm for 3 min and the fixation fluid was removed. Prior to analysis, cells were incubated with prepared staining solution (450 μL PI mixed with 50 μL RNase A) for 40 min in the dark. In the end, the fluorescence signal of cells was measured by an IFC (Amnis, Flow sight, USA) with background subtraction. The cell cycle distribution was analyzed by IDEAS software (version 6.2).

2.11. Animal Protocol. Female BALB/c mice aged nearly 6 weeks (20–25 g in weight) were purchased from the Beijing HFK Bioscience Co., Ltd. 4T1 tumor models were established by the subcutaneous injection (1×10^7 cells/mL, 200 μL per mouse) into the right hind leg of the mice. After 1 week, the tumor can grow to 50–70 mm^3. All the animal care and experimental procedures were conducted in accordance with the Animal Management Rules and Guidelines of the Ministry of Health of the People's Republic of China and approved by the Animal Ethics Committee of Jiangsu Normal University and Bengbu Medical College.

2.12. In Vivo Fluorescence Imaging. The real-time tumor-targeting capability of NR@RGD QDs was detected by an *in vivo* IVIS fluorescence imaging system (Caliper Life Sciences, USA) with the excitation of 570 nm filter and emission of 660 nm filter. The mice were intravenously administrated at a dosage of 1 mg As·kg^{-1} body weight for fluorescence-imaging scanning. Prior to fluorescence imaging, mice were anesthetized by inhaling isoflurane (1.5%) through the nose and the normal body temperature was maintained. Then, the in situ fluorescence imaging scanning was performed at different time points and the targeting ability of NR@RGD QDs was quantitatively evaluated by CI (CI = I_T/I_M) value which was calculated

by average fluorescence signal of tumor area (I_T) and adjacent normal muscle (I_M). After intravenous injection of NR@RGD QDs, mice were euthanized at specific points (4 and 24 hr) and the main organs (heart, liver, spleen, lung, kidney, and tumor) were extracted to measure the *ex vivo* fluorescence.

2.13. Immunofluorescent Staining of Tumor Vascularization. At 4 hr postinjection of NR@RGD QDs, tumor tissue was stripped from the euthanized mice and immediately fixed with a 4% paraformaldehyde solution overnight. Then, the tumor tissue was dehydrated in an ethanol solution with different concentration gradients (from 25% to 100%) and cut into small pieces. After washing with PBS three times, the tumor section was stained with DAPI (blue fluorescence signal points, CD31 marked) in the dark and then observed under CLSM monitoring.

2.14. In Vivo Antitumor Efficacy Evaluation. The 4T1 tumor-bearing mice were randomly divided into two groups ($n = 6$ per group), which were intravenously injected with saline and NR@RGD QDs, respectively. The evaluation index of antitumor effect in mice was mainly statistical with the changes of tumor volume and mice weight during a 16-day observation period. The volume of tumor was calculated by the following formula: $V = AB^2\pi/6$ (A represents the length and B represents the width).

2.15. Western Blot (WB) Assay. WB assay was used to detect the expression levels of cancer-related proteins. Here the tumor tissues were lysed on ice with RIPA (Applygen, Beijing, China) buffer mixing 1% phenylmethylsulfonyl fluoride for 30 min. The BCA assay kit (Pierce Biotechnology, Inc., Rockford, IL, USA) was used to quantitatively calculate the concentration of extracted protein samples. Equal amounts of protein were separated by 8%–12% SDS-PAGE and then transferred to the PVDF membrane. Subsequently, the membrane was blocked with 5% bovine serum albumin (BSA) for 1 hr followed by incubation with specific primary antibodies against anti-VEGFA and anti-β-actin (1 : 1,000; Cell Signaling Technology, Inc., Beverly, MA, USA) at 4°C overnight. After being washed with TBST three times, the membrane was incubated with secondary horseradish peroxide (HRP) conjugated antibodies against mouse or rabbit IgG (1 : 5,000; Cell Signaling Technology, Inc.) for 1.5 hr. The blots of protein were visualized by enhanced ECL chemiluminescence detection kit (Pierce Biotechnology, Inc.), and the images of targeted bands were captured by an automatic chemiluminescence imaging analysis system (Amersham Imager 600, General Electric Company, MA, USA). The protein expression was quantitatively analyzed by ImageJ software (Version 1.52v, National Institutes of Health, Bethesda, MD, USA).

2.16. Hematology Examination. Hematology examination was carried out to analyze the blood routine and liver/kidney function indicators. The blood-routine-associated indicators include white blood cells, red blood cells, hemoglobin, hematocrit, erythrocyte mean corpuscular volume, mean corpuscular hemoglobin, mean corpuscular concentration, blood platelet, aspartate aminotransferase, alkaline phosphatase, albumin, blood urea nitrogen, and creatinine were counted by an automated blood counter system.

2.17. Histological Examination. On the 16th day, the 4T1 tumor-bearing mice were executed and the related organs (heart, liver, spleen, lung, kidney, and tumor) were taken out immediately. The excised organs were fixed in 4% paraformaldehyde and dehydrated with gradient ethanol, and then embedded in paraffin. After deparaffinization and rehydration, the paraffin sections were subjected to conventional hematoxylin and eosin (H&E) staining and sealed with neutral gum. The histological analysis was performed using an optical microscope (Leica, DM4000 B, Germany).

In immunohistochemical (IHC) staining, the tumor sections embedded in paraffin were deparaffinized and dehydrated with gradient ethanol and then placed in citric acid buffer solution for antigen retrieval. Prior to the detection of the immune response, the HRP enzyme was inactivated by adding hydrogen peroxide working solution and blocked with goat serum blocking solution. Subsequently, tumor sections were sequentially incubated with primary antibodies (CD31 and Ki-67) and HRP-labeled goat anti-rabbit secondary antibody. After being washed with PBS, DAB chromogenic solution was added and then the reaction was halted at the appropriate shade. Subsequently, sections were restained with hematoxylin dye for 5 min. After being washed with distilled water, sections were sealed and observed under an optical microscope (Leica, DM4000 B).

In TUNEL staining, the apoptosis level of tumor cells was evaluated by a TUNEL detection kit. After being deparaffinized in xylene and hydrated with gradient ethanol, the tumor sections were reacted with proteinase K working solution at 37°C for 30 min, and then blocked with 3% H_2O_2 for 10 min. Subsequently, the sections were incubated with TdT enzyme reaction solution in the dark for 60 min. After being washed with PBS three times, sections were reacted with added streptavidin-HRP working solution in the dark at 37°C for 30 min. Finally, sections were incubated with DAB chromogenic solution until appropriate color emerged and then restained with hematoxylin dye for 10 min. Sections sealed with neutral gum were observed under an optical microscope (Leica, DM4000 B).

In Masson's trichrome staining, the degree of tumor collagen and muscle fiber lesions was determined using Masson's triple staining kit. Deparaffinized and rehydrated tumor sections were first incubated with hematoxylin staining solution for 5 min and then incubated with composite staining solution for another 5 min. After washing the staining solution, sections were stained with phosphomolybdic acid for 1 min and bright green staining solution for 5 min, respectively. The dried slices were sealed and observed under an optical microscope (Leica, DM4000 B).

3. Results and Discussion

3.1. Formation Mechanism and Characterization of NR@RGD QDs. We previously reported that the NR@EA CUs were less stable in acidic solutions in which the pH-sensitive protonation effect could interrupt the chemical chelation between
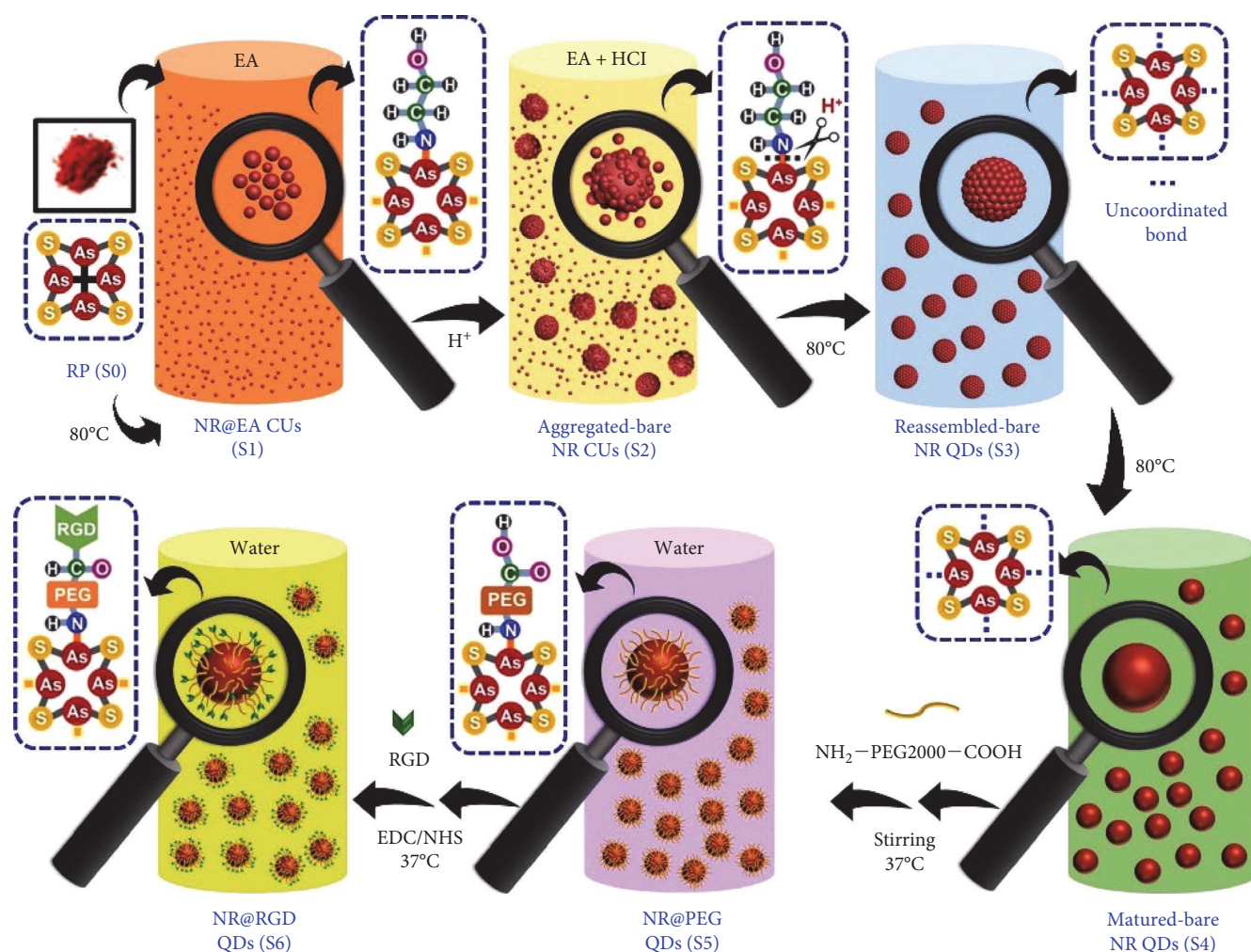
FIGURE 1: Schematic illustration of the synthetic process of NR@RGD QDs.

EA and arsenic atoms [22]. As a result, many aggregated-bare NR CUs precipitated from the NR@EA CUs solution in the presence of HCl, reducing the negative influence of EA. Interestingly, we found that the bare NR CUs continued to reassemble and grow into mature NR QDs of large sizes at 80°C. Figure 1 shows a schematic illustration of the stages in the formation of NR QDs from the initial NR CUs and NR aggregates that were also observed in the TEM images (Figure 2(a) and Supplementary Figure S1).

In recent years, research has shown that nanoclusters with aggregation-induced emission play a crucial role in the development of biomedicine and biosensors [23]. The obtained NR CUs and reassembled or matured NR QDs displayed excellent fluorescence emission characteristics ranging from 590 to 609 nm, as shown in Figure 2(b). During nucleation and growth, these irregular NR CUs became tighter, and with prolonged maturation duration, NR crystals with noticeably enhanced emission were observed. To clarify the nature of the emission-enhancement behavior, the crystalline characteristics of the NR CUs and NR QDs were further investigated by X-ray diffraction, as shown in Figure 2(c). Clear crystalline peaks gradually appeared during the formation of NR QDs.

The excellent optical properties of the NR QDs were associated with their crystal structure, in which the smaller NR CUs could easily facilitate self-assembly, complete structural optimization, and ultimately form regular crystals with a size quantization effect, leading to emission enhancement.

To obtain high-performance NR QDs with good biocompatibility and tolerability in the body, the as-prepared NR precipitate was centrifuged and redissolved in water by the As–N bonding reaction of functionalized NH_2–PEG2000–COOH and further coupled with RGD molecules to the carboxyl terminus, eventually forming water-soluble NR@RGD QDs (Figure 1). RGD peptides have excellent biocompatibility, can specifically bind to overexpressed receptors (e.g., integrin $\alpha_v\beta_3$) of various cancer cells, and have been used as targeted therapeutic agents for macromolecular prodrugs [24, 25]. Integrin $\alpha_v\beta_3$ can activate endothelial cells involved in tumor angiogenesis and regulate cancer cell proliferation and migration, and the uncontrollable growth and metastasis of tumor cells are closely related to tumor neovascularization [24–26]. Here, we expected that the functional NR@RGD QDs can anchor into the tumor endothelial cells through an active targeting effect, inhibit the angiogenesis in the
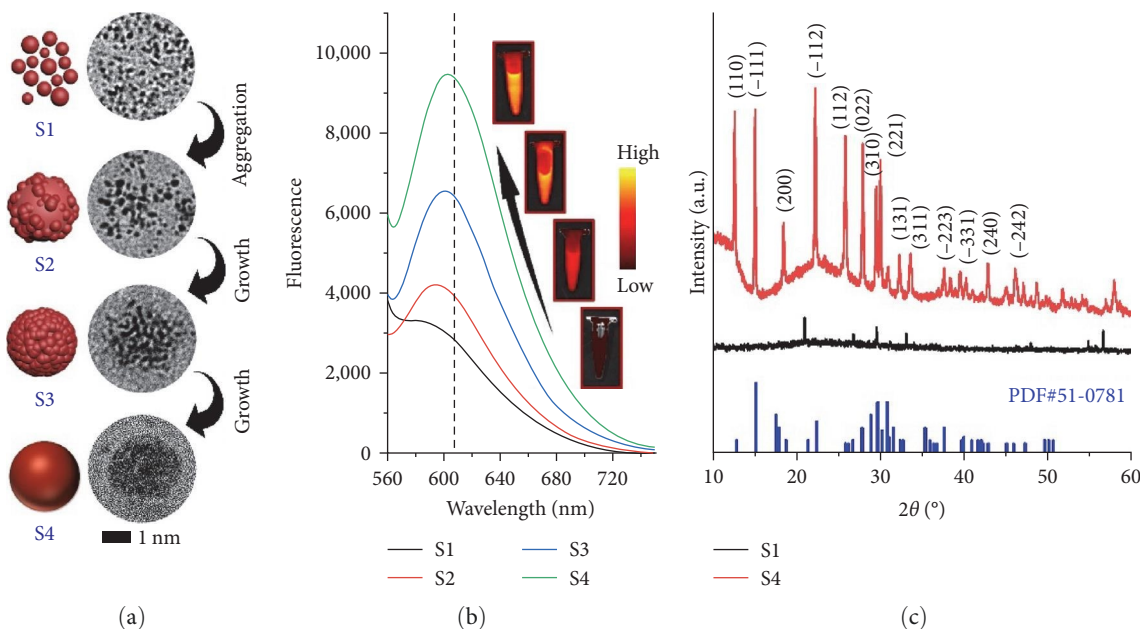
FIGURE 2: (a) Representative TEM images of NR QDs (S4) formation and transformation process from initial NR CUs (S1) and NR aggregates (S2, S3); (b) fluorescence characteristics; (c) XRD patterns of S1 and S4 samples withdrawn from the reaction process.

tumor, "cut-off" the nutrient-rich blood supply to tumors, and directly kill the cancer cells.

TEM examination revealed that the NR@RGD QDs had a well-defined spherical shape with an average size of 2–4 nm (Figure 3(a)). Clear lattice fringes (0.299 nm) were observed in the high-resolution TEM image of NR@RGD QDs, corresponding to the (221) lattice planes, which further revealed their high-quality crystalline nature. The corresponding hydrodynamic diameter (HD) of the NR@RGD QDs measured using dynamic light scattering was ~79.8 nm (Figure 3(b)). Notably, the NR@RGD QDs did not exhibit significant HD changes even after being maintained in a neutral aqueous solution (pH 7.4) for 4 weeks, demonstrating good colloidal stability (Supplementary Figure S2). Raman spectroscopy was used to study the structure of NR@RGD QDs, as shown in Figure 3(c). The Raman characteristic peaks of the NR@RGD QDs consisted of three regions: As–S stretching at 341 cm^{-1}, As–S–As bending at 225 cm^{-1}, and As–As stretching at 190 cm^{-1}, which verified the nature of the realgar. In addition, the NR@RGD QDs exhibited strong broadband characteristic UV–vis absorption within the range of 360–650 nm (Figure 3(d)). Meanwhile, a wide fluorescence emission region between 550 and 700 nm (the largest emission peak emerged at around 610 nm) was observed when the NR@RGD QDs were produced by optimal excitation (Figure 3(d)). Based on the wide absorption and unique emission characteristics, the NR@RGD QDs can show high potential *in vivo* bioimaging. To further evaluate the fluorescent stability, the NR@RGD QDs were exposed to dark (D), white-light irradiation (WI), and 808 nm laser irradiation (LI) for 6 hr (Figure 3(e)). As predicted, no obvious fluorescence loss was observed in either the WI or LI processes, and the fluorescence signal was maintained for 1 month, indicating that the NR@RGD QDs possessed high photostability and antilight quenching properties. Preliminary biocompatibility

evaluation of the NR@RGD QDs was performed using a hemolysis assay. As shown in Figure 3(f), no significant hemolysis was observed in the presence of NR@RGD QDs at various concentrations for 12 hr, indicating that the NR@RGD QDs have good biological compatibility, which provides an advantage for subsequent *in vitro* and *in vivo* applications.

3.2. In Vitro Cytotoxicity and Targeting Effects. To evaluate the *in vitro* antitumor activity of NR@RGD QDs, we first investigated the dose-dependent cytotoxicity in mouse breast cancer (4T1) cells using CCK-8 assays (Figure 4(a)). As the NR@RGD QDs concentration increased, the survival rate of cells showed a gradient decline. The 50% lethal concentration of NR@RGD QDs for 4T1 cells was 1.68 μg As·mL^{-1}, indicating that NR@RGD QDs had an excellent inhibitory effect on cell proliferation *in vitro*. To verify the intracellular trafficking and targeting behavior of NR@RGD QDs, human umbilical vein endothelial cells (HUVECs, high expression of integrin $\alpha_v\beta_3$) were selected as an *in vitro* model (Figure 4(b)) for fluorescence imaging detected by CLSM. Owing to the excellent fluorescence performance of NR@RGD QDs, strong red fluorescence signals were observed in HUVECs, indicating that the cellular internalization of NR@RGD QDs was mediated by receptor-mediated endocytosis. Reducing the nonspecific uptake of NR@RGD QDs by the mononuclear phagocyte system (MPS) in blood circulation is a key factor for long-term circulation *in vivo*. RAW 264.7 macrophages were selected to verify the antiphagocytic effect of NR@RGD QDs with an internal coupling of PEG molecular chains (Supplementary Figure S3). Compared with that of the positive NR@EA QDs group, almost no obvious red fluorescence signals were observed in the cytoplasmic regions of cells in the NR@RGD QDs group. The *in vitro* antiphagocytic effect provided strong evidence for the subsequent *in vivo* anti-MPS uptake ability of the NR@RGD QDs. Apoptosis induction and
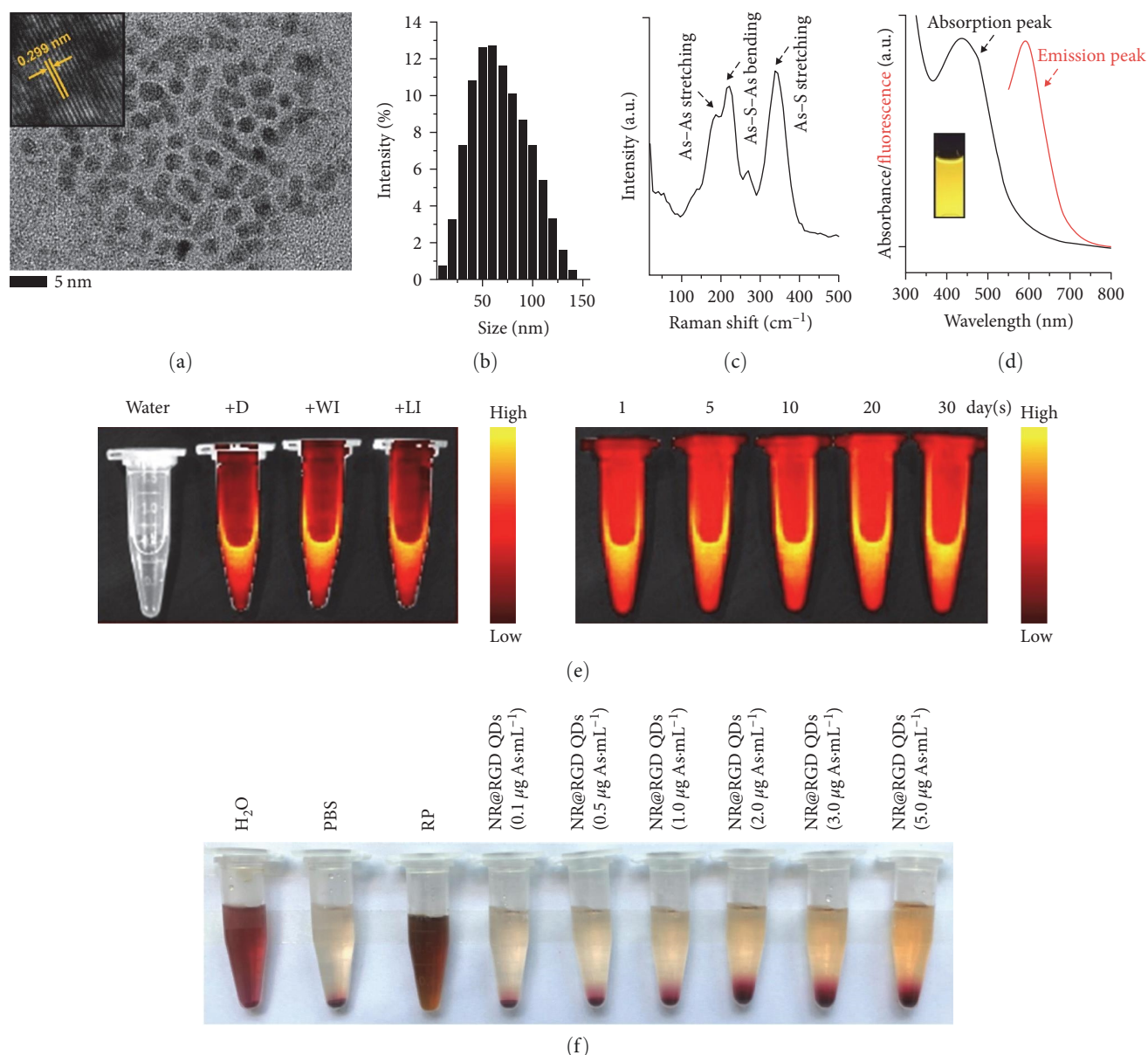
FIGURE 3: (a) TEM image (inset HRTEM image); (b) size distribution; (c) Raman spectroscopy; (d) UV−vis absorption (black line, inset strong fluorescent signal irradiated by UV light) and fluorescence spectra (red line); (e) fluorescent photographs; (f) *in vitro* hemolysis test of NR@RGD QDs.

cell cycle arrest are two major ways to inhibit tumor cell growth and proliferation [27]. The cytotoxicity of NR@RGD QDs on 4T1 cells was detected by immunofluorescent cell with FITC-Annexin V and PI double-fluorescence labeling (Figures 4(c) and 4(d)). The apoptotic rates in 4T1 cells are calculated as the total percentage of early and late apoptosis cells (indicated by LR and UR in a quadrantal diagram). Notably, NR@RGD QDs treatment led to a higher apoptosis rate (37.30%) than the untreated cells (3.30%) and simultaneously led to a marked increase of 20% in the proportion of cells (G2/M phase) (Supplementary Figure S4). After a series of *in vitro* studies, we have found that NR@RGD QDs could block the 4T1 cell cycle interference and induce apoptotic pathways, consequently suppressing cell proliferation. The

above-mentioned IFC tests indicate that NR@RGD QDs have significant *in vitro* antitumor activity.

3.3. In Vivo Real-Time Imaging and Targeting Behaviors.

We studied the *in vivo* circulation potential of the NR@RGD QDs and their active targeting of tumor neovascularization. BALB/c mice with subcutaneously transplanted 4T1 cells as tumor models were used to investigate the *in vivo* behavior of QDs in which the mice were intravenously injected with a single NR@RGD QDs administration (200 μL, 1 mg As·kg^{-1} body weight). *In vivo* fluorescence imaging was conducted for the mice by recording the QDS fluorescence signals at 1, 2, 4, 6, 8, 12, and 24 hr, as shown in Figure 5(a). To quantitatively determine the targeting effect of NR@RGD
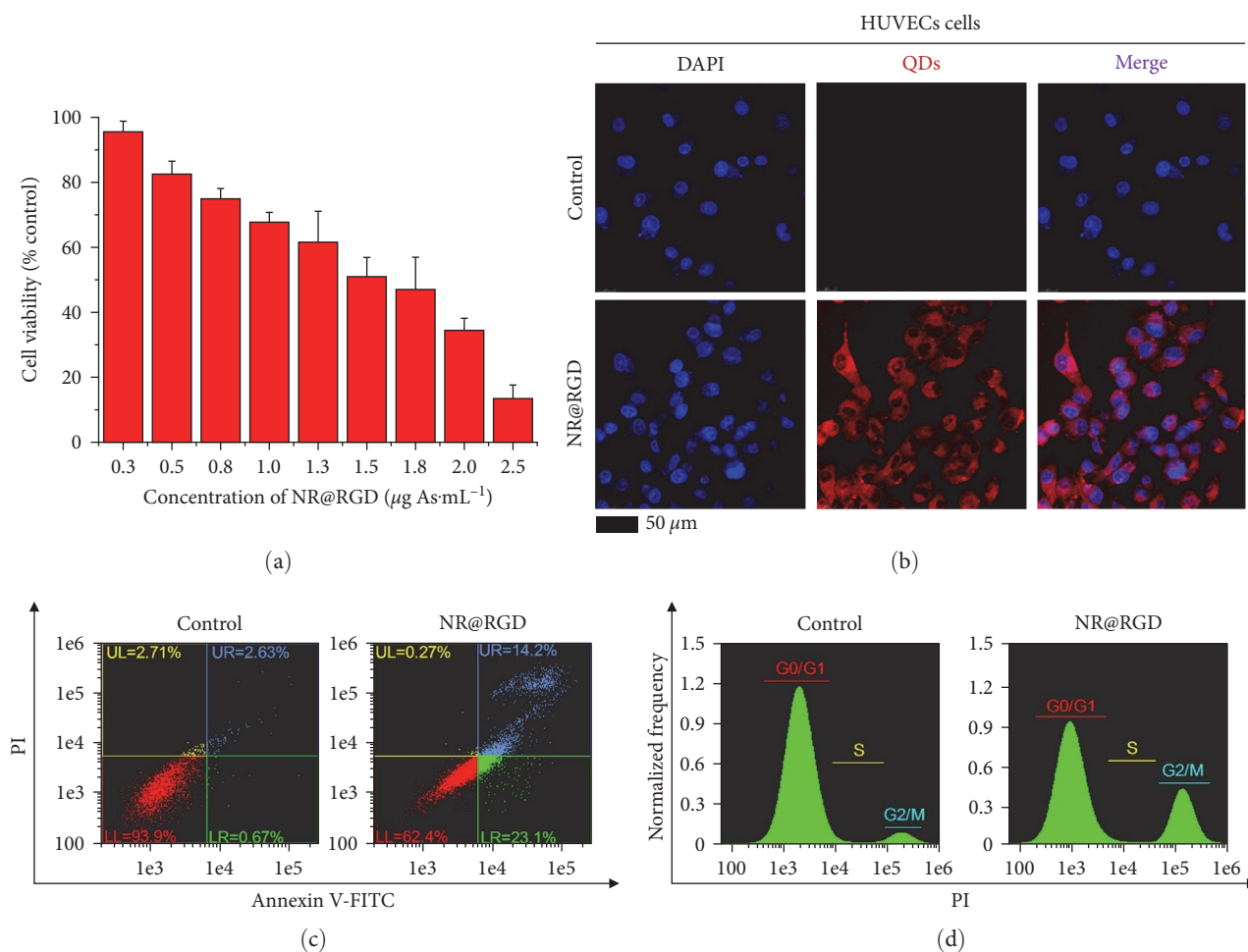
(a)

(b)

(c)

(d)

FIGURE 4: (a) CCK-8 assay of 4T1 cells treated with NR@RGD QDs at different concentrations for 24 hr; (b) CLSM images of DAPI-stained 4T1 cells after being treated with NR@RGD QDs ($1.0\,\mu g$ of As·mL^{-1}); (c) apoptosis/necrosis rate; (d) cell cycle distribution of 4T1 cells after being treated with NR@RGD QDs detected by IFC ($1.0\,\mu g$ of As·mL^{-1}).

QDs, we calculated the mean signal contrast index (CI) in the tumor region and adjacent muscle tissue of mice (a CI threshold of 2.5 was generally considered substantial evidence for an effective tumor-targeting effect [28]) (Figure 5(b)). After NR@RGD QDs administration, the fluorescence signal in the tumor area (white arrow) significantly increased and reached maximal fluorescence intensity for a duration of 4 hr, indicating the maximum accumulation of QDs. In the following 4–24 hr, the fluorescence signal gradually weakened because of the metabolism and clearance of the liver and kidneys. Meanwhile, the main organs (heart, liver, spleen, lung, and kidney) and tumors were dissected at 4 and 24 hr postinjection and immediately collected for further *ex vivo* fluorescence imaging (Figure 5(c)). As expected, among all organs, the highest fluorescence signal of QDs was observed in tumors at 4 hr postinjection. Our statistical results also showed that the CI values of the tumor region in NR@RGD QDs administration were >2.5 within 2–12 hr (Figure 5(b)). The subsequent immunofluorescent staining of tumor slices indicated that the NR@RGD QDs (red fluorescence signal points) were gathered in tumor-branched or circular vascularization (blue fluorescence signal points, CD31 stained), which provided

strong evidence for excellent tumor vascular targeting ability (Figure 5(d)). Based on these findings, we concluded that NR@RGD QDs could preferably penetrate solid tumor tissues through the enhanced permeability and retention effect (passive targeting) and enhanced vascular targeting ability (active targeting), achieving efficient accumulation at tumor sites (Figure 5(e)). The high efficiency of tumor neovascular targeting is an essential precondition for effective chemotherapeutic processes in the future.

3.4. In Vivo Antitumor Therapy. To achieve the long-term antitumor efficacy of NR@RGD QDs *in vivo*, we designed an optimized tumor treatment strategy in which saline and NR@RGD QDs were administrated to mice via the tail vein every 3 days for 16 days of treatment at a concentration of 5 mg As·kg^{-1} body weight. Tumor volumes and body weights of the mice were recorded during treatment. Notably, the body weights of the mice in the saline and NR@RGD QDs treatment groups were not significantly different, indicating that the mice tolerated repeated NR QDs administrations (Figure 6(a)). In comparison, mice treated with NR@RGD QDs receiving targeted tumor vasculature penetration
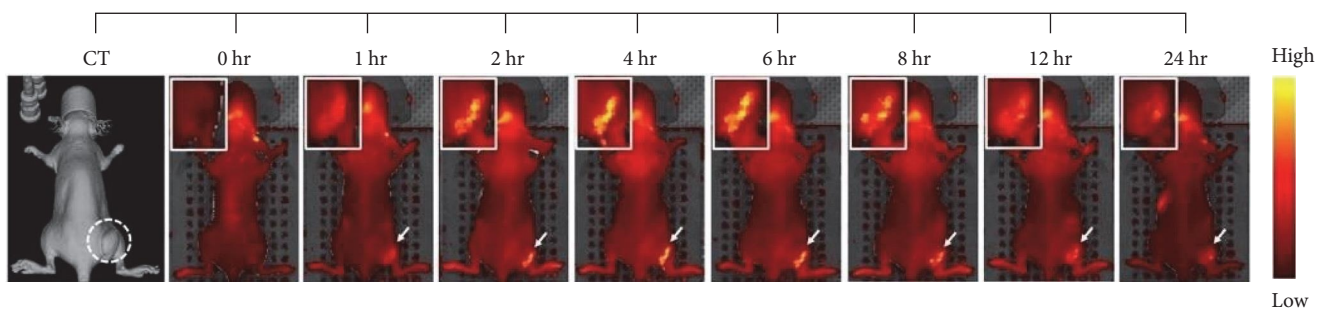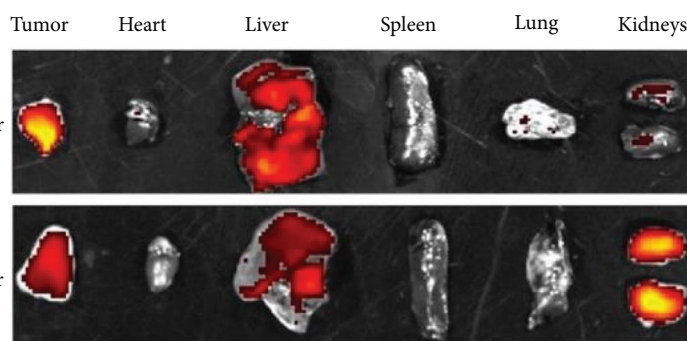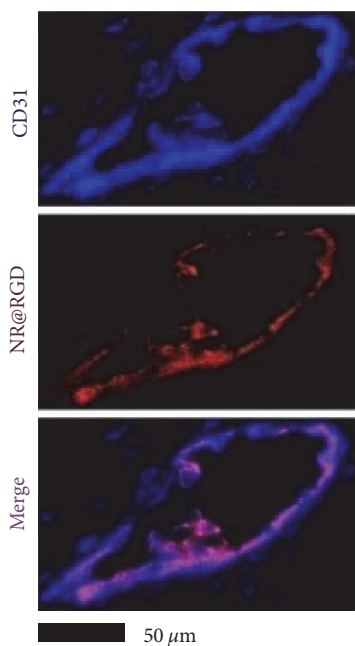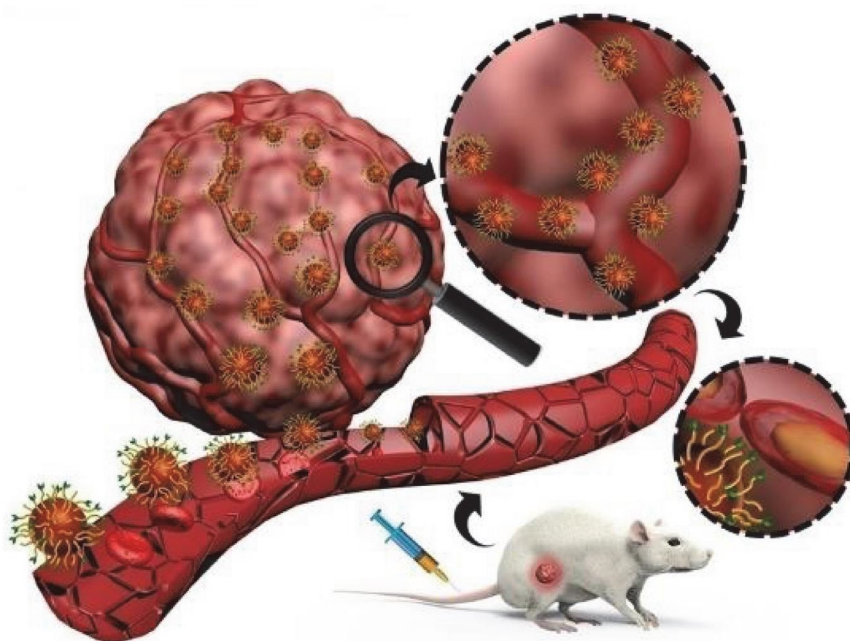
(a)
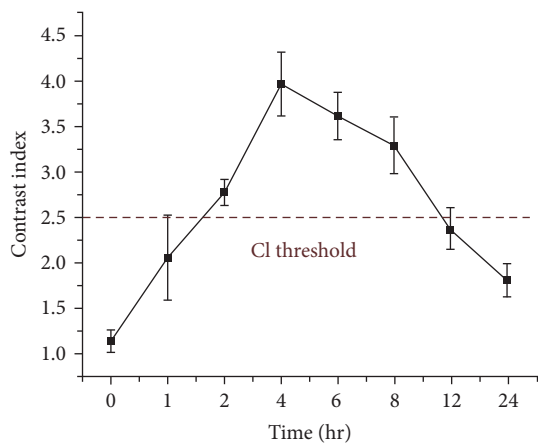
(b)

(c)

(d)

(e)

FIGURE 5: (a) *In vivo* fluorescence imaging ($E_x = 570$ nm, $E_m = 660$ nm) of tumor-bearing mice after intravenous injection of NR@RGD QDs (1 mg As·kg^{-1} body weight); (b) corresponding fluorescence CI changes at the tumor sites and adjacent muscle tissue at different times; (c) *ex vivo* fluorescence images of major normal organs (heart, liver, spleen, lung, and kidneys) and tumor tissues after injection of NR@RGD QDs collected at 4 and 24 hr; (d) CLSM images for tumor vascularization after treatment with NR@RGD QDs; (e) schematic illustration of NR@RGD QDs-mediated tumor vascular targeting therapy.
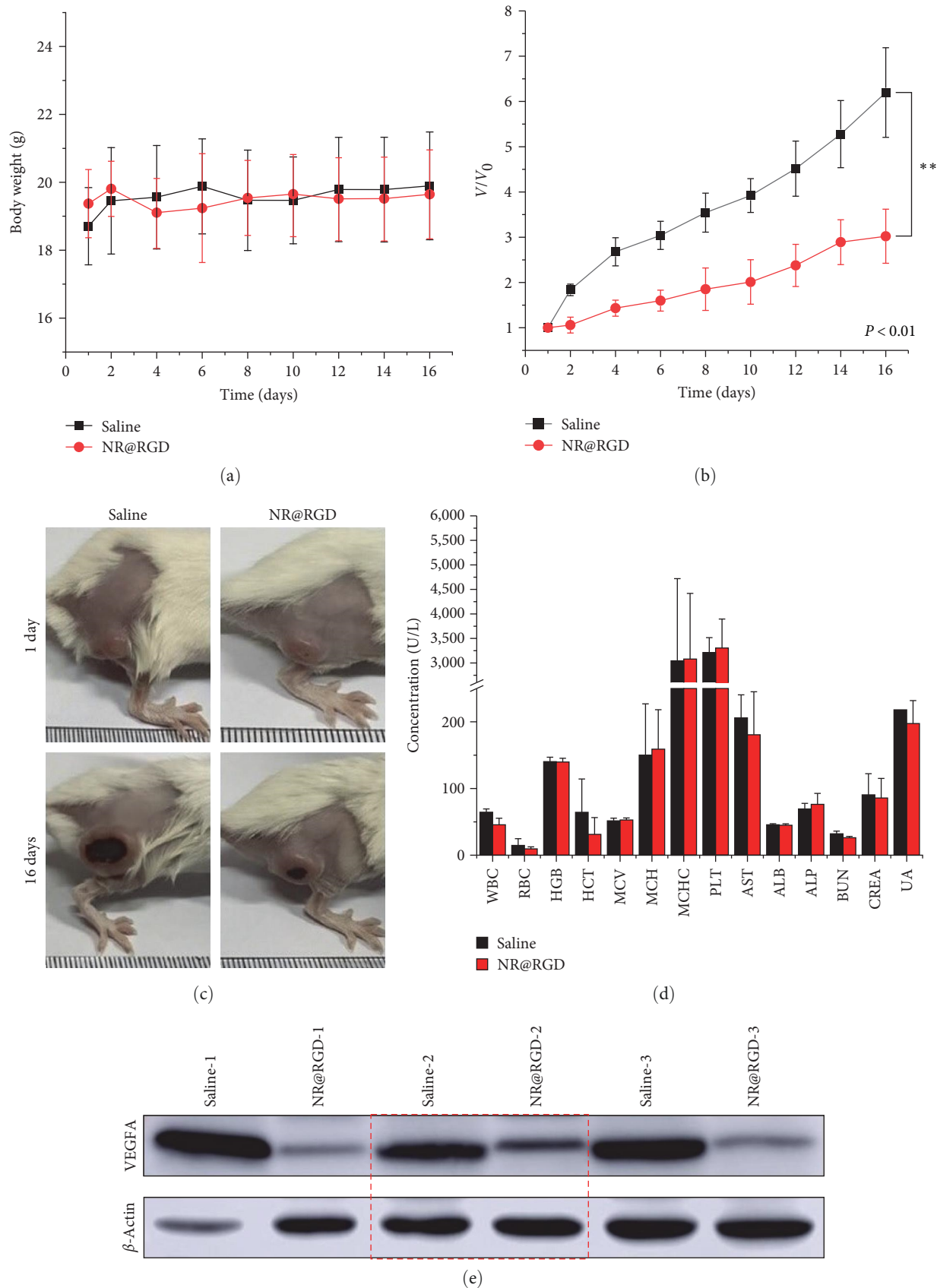
(a)

(b)

(c)

(d)

(e)

FIGURE 6: (a) Body weight changes; (b) tumor growth rates; (c) photographic images of mice during the treatment of saline and NR@RGD QDs for 16 days ($n = 6$); (d) blood routine and liver/kidney function indicators of mice; (e) the expression of VEGFA protein in tumor tissues by using WB analysis. β-Actin served as loading control. The partial electrophoretic gel imaging has been circled for comparison displayed in red.
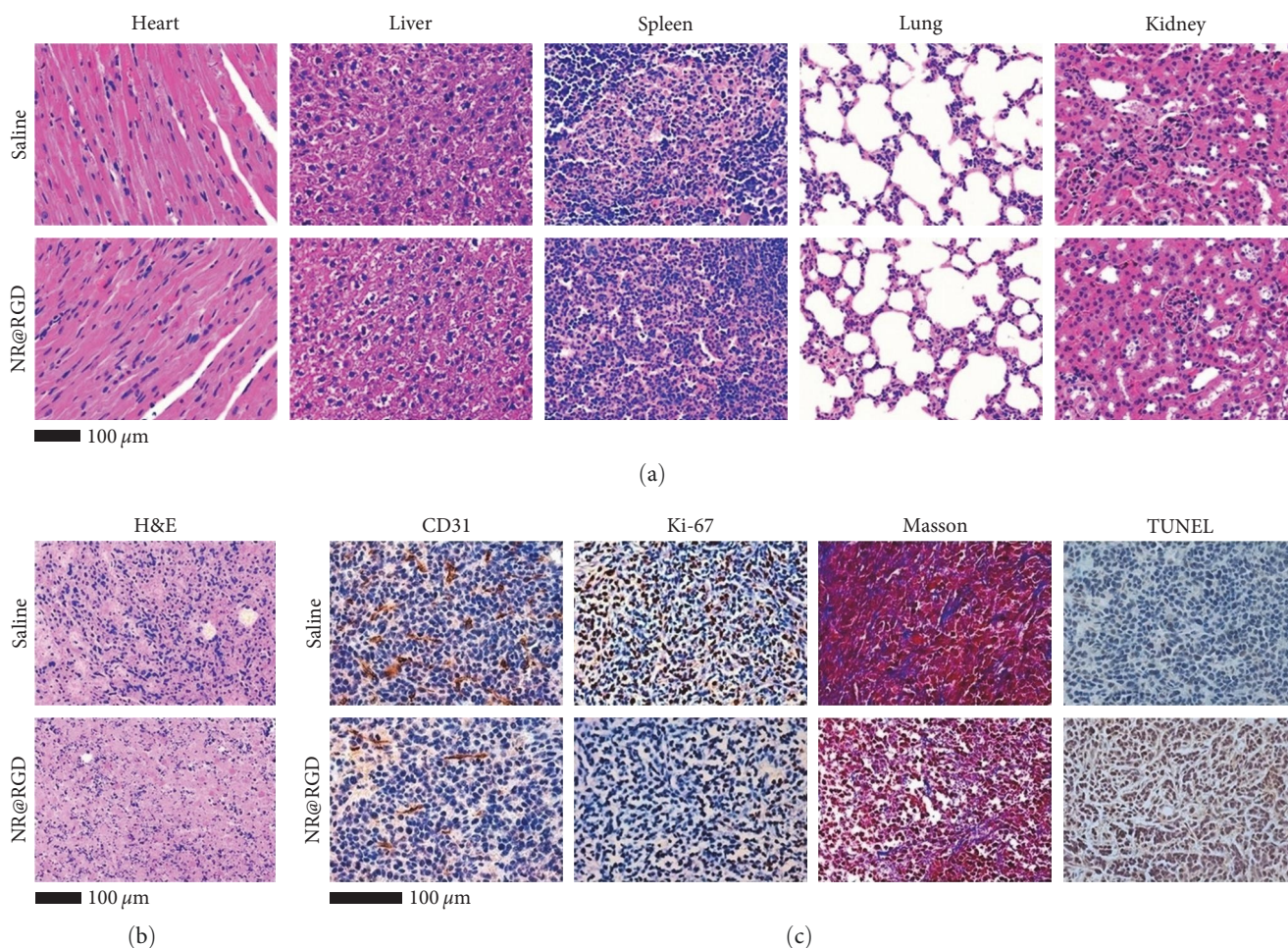
(a)

(b)

(c)

FIGURE 7: H&E staining images of (a) mice major normal organs (heart, liver, spleen, lung, and kidneys) and (b) tumor sections stripped from mice after the treatment of saline and NR@RGD QDs on the 16th day. (c) Tumor sections stripped from mice on the 16th day stained with common IHC (CD31 and Ki-67), Masson, and TUNEL.

exhibited significant tumor inhibition efficacy (Figures 6(b) and 6(c)). All hematological indices and liver/kidney function indicators (AST, ALP, ALT, BUN, and CREA) of the mice were within normal levels, indicating that the NR@RGD QDs have good blood compatibility (Figure 6(d)).

Subsequently, the mice were euthanized, and the related organs or tissues (tumor, heart, liver, spleen, lung, and kidney) were used for histopathological and related protein analysis. Generally, some tumor neovascular indexes rather than tumor size are more reliable prognostic indicators for tumor after the chemotherapy of NR@RGD QDs. Based on the excellent tumor neovascular targeting ability of NR@RGD QDs, we carried out a WB assay of tumor neovascularization-related proteins to determine the mechanisms underlying the antitumor effects, as shown in Figure 6(e) and Supplementary Figure S5. Vascular endothelial growth factor A (VEGFA), secreted by numerous tumor cells, plays a crucial role in the promotion of tumor angiogenesis and metastasis [29, 30]. As predicted, VEGFA expression levels in tumors treated with NR@RGD QDs were significantly lower than those in the saline group, confirming that the NR@RGD QDs could effectively inhibit tumor angiogenesis, suppressing tumor migration and invasion through inhibiting VEGFA-dependent signaling pathway.

To evaluate the tumor antiangiogenic and apoptotic effects of NR@RGD QDs, we immediately performed H&E staining and IHC staining of tumor angiogenesis, cell migration- and proliferation-associated protein (CD31 and Ki-67), and TUNEL staining of tumor sections. H&E staining results indicated that NR@RGD QDs could induce more cell structural damage in tumor tissues than the saline group, including decreased cell density, nuclear shrinkage, and fragmentation, without adverse effects in normal tissue (Figures 7(a) and 7(b)). IHC staining results (Figure 7(c)) showed that CD31 and Ki-67 protein expression levels (marked brown) were higher in the saline group but significantly decreased in the NR@RGD QDs group. The results of tumor antiangiogenic effects-mediated IHC here are consistent with the aforementioned *in vivo* WB results. In addition, the NR@RGD QD-induced antiangiogenic therapy presented more numbers of TUNEL-apoptotic tumor cells with brown staining than the saline group. Masson's trichrome staining was conducted on dense collagen deposition or collagenous fibers (blue-stained) and muscle fibers (red-stained) in the tumor tissue. Collagen fibers could serve as a

"nutrition bank" to provide a sufficient supply of nutrients for tumor growth, while muscle fibers could play a critical role in maintaining tumor morphology. Masson's staining results indicated that NR@RGD QDs inhibited cell proliferation and migration by suppressing tumor collagen and muscle fiber growth, disturbed the tumor microenvironment balance, and eventually achieved their anticancer potential.

4. Conclusion

In summary, we developed functional NR@RGD QDs with enhanced fluorescence characteristics by CU-aggregation-induced crystal structure optimization for tumor neovascular targeting-associated theranostics. As an accurate-targeting drug delivery system, the NR@RGD QDs combined diagnostic and therapeutic functions within a single nanoplatform; they were used as a fluorescence probe for medical diagnosis as well as a chemotherapeutic agent for tumor treatment. Under the guidance of the active targeting effect, NR@RGD QDs penetrated the tumor-fenestrated vascular networks, effectively inhibited the growth of new tumor blood vessels, reduced cell proliferation and migration, and slowed tumor growth. By varying the dosage form of realgar, the potential advantages of "old medicine for new use" in TCM may provide a new direction for future clinical practice.

Data Availability

The data used to support the findings of this study are included within the article and in supplementary information file(s).

Conflicts of Interest

The authors declare that they have no conflicts of interest.

Authors' Contributions

Shengyan Pu, Wenwen Wu, and Jun Xie wrote the manuscript. Jun Xie, Yu Yan, and Xinqi Wang designed the project. Shengyan Pu, Wenwen Wu, Dongsheng Shi, Yanqi Dai, Jun Zhang, Mingyan Zhao, and Shuangyu Liu performed the experiments and analyzed the results. Guihong Zheng provided useful suggestions to this work.

Shengyan Pu and Wenwen Wu contributed equally to this work.

Funding

Supplementary Materials

Figures S1−S5 showing supplementary TEM images of the total stages in the formation of NR QDs from initial NR CUs and NR aggregates, the HD changing curves of NR@RGD QDs at pH 7.4 in 4 weeks, *in vitro* phagocytosis behavior of NR@RGD QDs and NR@EA QDs on RAW 264.7 macrophages, corresponding cell cycle graphical representation of 4T1 cells treated with NR@RGD QDs and quantification of indicated VEGFA protein/β-actin in WB assay. (*Supplementary Materials*)

References

[1] J. Shi, P. W. Kantoff, R. Wooster, and O. C. Farokhzad, "Cancer nanomedicine: progress, challenges and opportunities," *Nature Reviews Cancer*, vol. 17, pp. 20–37, 2017.

[2] M. Jia, T. Wang, S. Xu et al., "Arsenic sulfide nanoformulation induces megakaryocytic differentiation through histone deacetylase inhibition," *Advanced Therapeutics*, vol. 3, no. 5, Article ID 1900151, 2020.

[3] P. J. Dilda and P. J. Hogg, "Arsenical-based cancer drugs," *Cancer Treatment Reviews*, vol. 33, no. 6, pp. 542–546, 2007.

[4] Z. Cui, Y. Zhang, K. Xia et al., "Nanodiamond autophagy inhibitor allosterically improves the arsenical-based therapy of solid tumors," *Nature Communications*, vol. 9, Article ID 4347, 2018.

[5] T. Wang, J. Meng, C. Wang et al., "Inhibition of murine breast cancer metastases by hydrophilic As_4S_4 nanoparticles is associated with decreased ROS and HIF-1α downregulation," *Frontiers in Oncology*, vol. 9, Article ID 333, 2019.

[6] X. Wang, X. Zhong, J. Li, Z. Liu, and L. Cheng, "Inorganic nanomaterials with rapid clearance for biomedical applications," *Chemical Society Reviews*, vol. 50, no. 15, pp. 8669–8742, 2021.

[7] X. Wang, X. Wang, Q. Yue et al., "Liquid exfoliation of TiN nanodots as novel sonosensitizers for photothermal-enhanced sonodynamic therapy against cancer," *Nano Today*, vol. 39, Article ID 101170, 2021.

[8] M. Yin, X. Chen, Q. Guo et al., "Ultrasmall zirconium carbide nanodots for synergistic photothermal-radiotherapy of glioma," *Nanoscale*, vol. 14, no. 40, pp. 14935–14949, 2022.

[9] D. Liu, X. Dai, W. Zhang et al., "Liquid exfoliation of ultrasmall zirconium carbide nanodots as a noninflammatory photothermal agent in the treatment of glioma," *Biomaterials*, vol. 292, Article ID 121917, 2023.

[10] X. Dai, Y. Shao, X. Tian et al., "Fusion between glioma stem cells and mesenchymal stem cells promotes malignant progression in 3D-bioprinted models," *ACS Applied Materials & Interfaces*, vol. 14, no. 31, pp. 35344–35356, 2022.

[11] Q. Guo, M. Yin, J. Fan et al., "Peroxidase-mimicking TA-VO$_x$ nanobranches for enhanced photothermal/chemodynamic therapy of glioma by inhibiting the expression of HSP60," *Materials & Design*, vol. 224, Article ID 111366, 2022.

[12] P. Dai, W. Zhu, B. Yan et al., "Regulation of ID4 in vivo for efficient magnetothermal therapy of breast cancer," *Advanced Therapeutics*, vol. 4, no. 5, Article ID 2000291, 2021.

[13] T. Zhang, G. Li, Y. Miao et al., "Magnetothermal regulation of in vivo protein corona formation on magnetic nanoparticles for improved cancer nanotherapy," *Biomaterials*, vol. 276, Article ID 121021, 2021.

[14] D. Cholujova, Z. Bujnakova, E. Dutkova et al., "Realgar nanoparticles *versus* ATO arsenic compounds induce *in vitro* and *in vivo* activity *against* multiple myeloma," *British Journal of Haematology*, vol. 179, no. 5, pp. 756–771, 2017.

[15] H. Wang, Z. Liu, Y. Gou et al., "Apoptosis and necrosis induced by novel realgar quantum dots in human endometrial

cancer cells via endoplasmic reticulum stress signaling pathway," *International Journal of Nanomedicine*, vol. 10, no. 1, pp. 5505–5512, 2015.

[16] J. Z. Wu, G. Chen, Y. B. Shao et al., "Fluorescent realgar quantum dots: new life for an old drug," *Nano*, vol. 11, no. 1, Article ID 1650005, 2016.

[17] Y. An, Nie, W. Ziyu, and D. Zhang, "Preparation and characterization of realgar nanoparticles and their inhibitory effect on rat glioma cells," *International Journal of Nanomedicine*, vol. 6, pp. 3187–3194, 2011.

[18] D. Shi, Y. Liu, R. G. Xi et al., "Caveolin-1 contributes to realgar nanoparticle therapy in human chronic myelogenous leukemia K562 cells," *International Journal of Nanomedicine*, vol. 11, pp. 5823–5835, 2016.

[19] T. Wang, T. Wen, H. Li et al., "Arsenic sulfide nanoformulation induces erythroid differentiation in chronic myeloid leukemia cells through degradation of BCR-ABL," *International Journal of Nanomedicine*, vol. 14, pp. 5581–5594, 2019.

[20] J. Wang, M. Lin, T. Zhang et al., "Arsenic(II) sulfide quantum dots prepared by a wet process from its bulk," *Journal of the American Chemical Society*, vol. 130, no. 35, pp. 11596-11597, 2008.

[21] J. Wang, K. P. Loh, Z. Wang et al., "Fluorescent nanogel of arsenic sulfide nanoclusters," *Angewandte Chemie International Edition*, vol. 48, no. 34, pp. 6282–6285, 2009.

[22] D. Shi, S. Pu, H. Yin et al., "Fluorescent realgar nanoclusters for nuclear targeting-triggered tumor theranostics," *ACS Applied Nano Materials*, vol. 5, no. 5, pp. 6485–6499, 2022.

[23] T. Shi, C. Huang, Y. Li, F. Huang, and S. Yin, "NIR-II phototherapy agents with aggregation-induced emission characteristics for tumor imaging and therapy," *Biomaterials*, vol. 285, Article ID 121535, 2022.

[24] X. Shan, L. Zhang, Y. Xu et al., "An octopus-mimic PEGylated peptide as a specific integrin $\alpha_v\beta_3$ inhibitor for preventing tumor progression," *Chemical Communications*, vol. 56, no. 14, pp. 2178–2181, 2020.

[25] S. Liu, D. Shi, L. Chen et al., "Paclitaxel-loaded magnetic nanocrystals for tumor neovascular-targeted theranostics: an amplifying synergistic therapy combining magnetic hyperthermia with chemotherapy," *Nanoscale*, vol. 13, no. 6, pp. 3613–3626, 2021.

[26] J. S. Desgrosellier, L. A. Barnes, D. J. Shields et al., "An integrin $\alpha_v\beta_3$–c-Src oncogenic unit promotes anchorage-independence and tumor progression," *Nature Medicine*, vol. 15, pp. 1163–1169, 2009.

[27] W. Wang, K. Chen, Y. Su, J. Zhang, M. Li, and J. Zhou, "Lysosome-independent intracellular drug/gene codelivery by lipoprotein-derived nanovector for synergistic apoptosis-inducing cancer-targeted therapy," *Biomacromolecules*, vol. 19, no. 2, pp. 438–448, 2018.

[28] X. Lai, L. Tan, X. Deng et al., "Coordinatively self-assembled luminescent gold nanoparticles: fluorescence turn-on system for high-efficiency passive tumor imaging," *ACS Applied Materials & Interfaces*, vol. 9, no. 6, pp. 5118–5127, 2017.

[29] P. Majumder, S. Bhunia, and A. Chaudhuri, "A lipid-based cell penetrating nano-assembly for RNAi-mediated anti-angiogenic cancer therapy," *Chemical Communications*, vol. 54, no. 12, pp. 1489–1492, 2018.

[30] A. AbdelHaleem, A. O. Mansour, M. AbdelKader, and R. K. Arafa, "Selective VEGFR-2 inhibitors: synthesis of pyridine derivatives, cytotoxicity and apoptosis induction profiling," *Bioorganic Chemistry*, vol. 103, Article ID 104222, 2020.